PCCP

PAPER

View Article Online
View Journal | View Issue

Cite this: *Phys. Chem. Chem. Phys.*, 2018, **20**, 27456

Atomistic determination of the surface structure of $Cu_2O(111)$: experiment and theory†

Rui Zhang, ‡[a] Liang Li, ‡[a] Laszlo Frazer, [bc] Kelvin B. Chang,[d] Kenneth R. Poeppelmeier, [de] Maria K. Y. Chan [a] and Jeffrey R. Guest *[a]

Received 25th September 2018,
Accepted 9th October 2018

DOI: 10.1039/c8cp06023a

rsc.li/pccp

Cuprous oxide (Cu_2O) is a promising catalyst for several important reactions. However, the atomic structures of defective Cu_2O surfaces, which critically affect the catalytic properties both thermodynamically and kinetically, are not unambiguously characterized. High-resolution scanning tunneling microscopy (STM), combined with density functional theory (DFT) calculations and STM simulations, has been used to determine the atomic structure of the (111) surface of a Cu_2O bulk crystal. The single crystal surface, processed by ultrahigh vacuum cleaning and oxygen annealing, shows a (1 × 1) periodicity in the low-energy electron diffraction pattern. The pristine (defect-free) $Cu_2O(111)$ surface exhibits a lattice of protrusions with hexagonal symmetry under STM, which is attributed to the dangling bonds of the coordinatively unsaturated copper (Cu_U) atoms on the surface. Two types of surface atomic defects are also identified, including the Cu_U vacancy and the oxygen-vacancy-induced local surface restructuring. The electronic structure of this surface measured by d*I*/d*V* spectroscopy shows an energy band gap of ~1.6–2.1 eV. Consistent with d*I*/d*V* measurements, DFT calculations identified surface states within the electronic band gap arising from the Cu ions on the surface. Our results provide a clear picture of the pristine and defective $Cu_2O(111)$ surface structure in addition to the formation mechanism of the reconstructed surface, paving the way toward studying the site-dependent reactivity of this surface.

Introduction

Cuprous oxide (Cu_2O) is a prototypical p-type semiconducting oxide with applications in photovoltaics[1–3] and photocatalysis.[4–9] The Cu^+ ions on Cu_2O single crystalline surfaces play an important role in the functioning of Cu-based photocatalysts,[10,11] which have been used in water–gas shift reactions for hydrogen production[12] and CO_2 reduction reactions for methanol synthesis.[11] Therefore, studying the surface structure of Cu_2O single crystals is helpful for the understanding of the process and mechanism of catalytic reactions taking place on the surface, and the unambiguous determination of the correct surface structure of Cu_2O surfaces is of particular importance for the demonstration of the site-dependent catalytic reactivity of the surface Cu ions that has been reported in several reactions.[13–15]

The oxygen-terminated $Cu_2O(111)$ surface has been found to be one of the most energetically stable single crystalline facets of Cu_2O,[16–18] but its exact surface termination, stoichiometry, and atomic structure still remain uncertain and have been the subjects of many recent experimental and theoretical investigations. The stoichiometric $Cu_2O(111)$ surface with the minimum surface energy is nonpolar and terminated by an outmost atomic layer of coordinatively unsaturated oxygen anions (O_U), with a second atomic layer of Cu^+ cations, and a third atomic layer of coordinatively saturated oxygen anions (O_S).[18] The Cu ions between the O_U and O_S layers on the stoichiometric $Cu_2O(111)$ surface can also be categorized into two groups depending on their local bonding environments, namely, coordinatively saturated copper ions (Cu_S) and coordinatively unsaturated copper ions (Cu_U) (Fig. 1a).[14] These surface sites act as an excellent platform for the study of site-dependent catalytic reactivity. The atomic structure of this surface has been theoretically studied by first-principles density functional theory (DFT) calculations,[10,13,14,16–19] which predicted that the (1 × 1) $Cu_2O(111)$ surface with missing Cu_U ions has the lowest surface energy while the stoichiometric surface shows a slightly higher energy than the Cu_U vacant surface under ultrahigh vacuum (UHV) conditions.[14,20] Spatially averaged experimental

[a] *Center for Nanoscale Materials, Argonne National Laboratory, 9700 South Cass Avenue, Argonne, IL 60439, USA. E-mail: jrguest@anl.gov*
[b] *Centre of Excellence in Exciton Science, UNSW, Sydney, NSW 2052, Australia*
[c] *Monash University, Clayton, Victoria 3800, Australia*
[d] *Department of Chemistry, Northwestern University, 2145 Sheridan Road, Evanston, IL 60208, USA*
[e] *Chemical Sciences and Engineering Division, Argonne National Laboratory, 9700 South Cass Avenue, Argonne, IL 60439, USA*

† Electronic supplementary information (ESI) available. See DOI: 10.1039/c8cp06023a

‡ These authors contributed equally to this work.

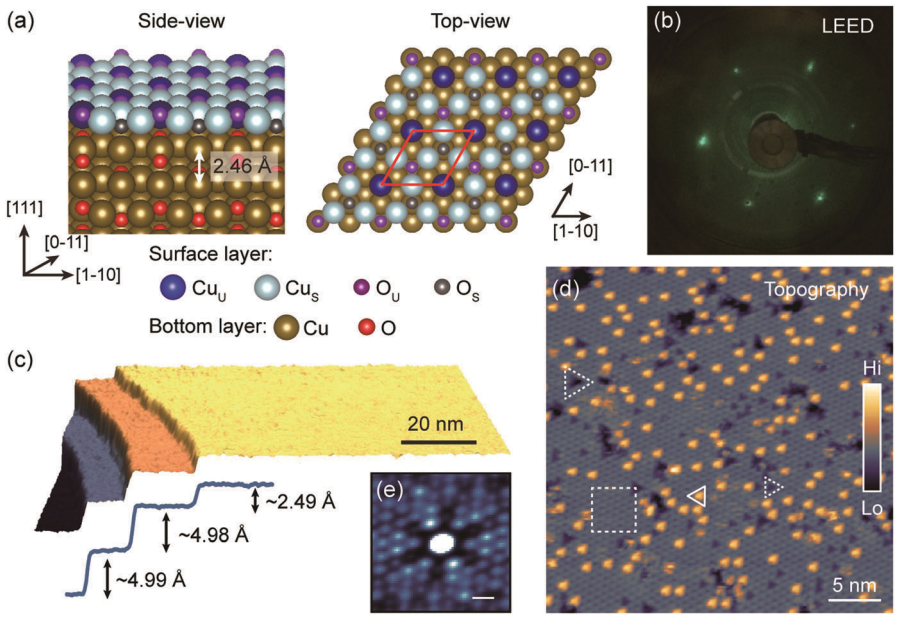

Fig. 1 Morphology of a single crystalline surface of $Cu_2O(111)$. (a) Model of the atomic structure of the stoichiometric $Cu_2O(111)$ surface. The interlayer distance along the [111] direction is 2.46 Å. (b) LEED pattern of the $Cu_2O(111)$ single crystal surface taken just after the UHV preparation. (c) Large-scale STM topographic image (+2 V, 20 pA) and the corresponding height profile of the atomic terraces of the $Cu_2O(111)$ surface. (d) High-resolution STM topographic image (−1.5 V, 30 pA, *z* range: 51 Å) showing three representative surface structures: the pristine surface region (dashed square), bright protrusions (solid triangle), and dark depressions (dashed triangle). (e) 2D autocorrelation analysis of data from (d); scale bar is 1 nm, details in the ESI.†

approaches using photoelectron spectroscopies and low-energy electron diffraction (LEED) have also been used to study the structure of this surface.[21] Two types of surface structures corresponding to (1×1) and $(\sqrt{3} \times \sqrt{3})R30^\circ$ periodicities were identified. The former corresponds to the pristine oxygen-terminated (111) surface, while the latter reconstruction is attributed to the removal of one-third of the surface oxygen anions.

Recently, scanning tunnelling microscopy (STM) has been used to directly access the surface and electronic structures of $Cu_2O(111)$ single crystals[22] and thin films.[23–25] The thin film samples, which consist of one[25] to a few[23,24] atomic layers on gold substrates, have revealed many insights into the surface terminations and strain-induced structuring; however, experiments on single crystals are critical to understand the structure, electronic structure, and native point defects away from doping and strain introduced by a nearby substrate, and without the confinement effects of a nm-scale film thickness.[24] On single crystals, Önsten *et al.*[22] successfully acquired both the (1×1) and $(\sqrt{3} \times \sqrt{3})R30^\circ$ reconstructed $Cu_2O(111)$ surfaces, and measured the surface topography of the latter reconstructed surface down to a sub-nanometer length scale. They proposed two possible atomic models for both surfaces. One of these is based on the stoichiometric (111) surface (with Cu_U ions), while the other is based on the stoichiometric surface without Cu_U ions. However, the exact atomic structure of this (111) surface could not be determined due to the limited resolution of the STM measurements. For a more complete understanding of the chemical properties of this surface, especially with respect to catalytic reactions, it is important to investigate the atomically resolved surface configuration as well as surface defects and their formation mechanisms.

In this work, we determine the $Cu_2O(111)$ surface atomic structure using STM in combination with DFT calculations and STM simulations. We demonstrate that the STM signal is dominated by unsaturated Cu atoms (Cu_U), and unambiguously identify and characterize defects due to both Cu_U and O_U vacancies at the atomic scale. We also perform scanning tunnelling spectroscopy (STS) studies and compare with DFT calculations of the electronic structure, and show that the surface atomic defect structures provide low-lying energy states, which may benefit the adsorption and/or reaction of gas molecules on this catalytically active surface. This characterization and understanding at the atomic scale are critical factors in the development of an accurate and complete picture of the surface reactivity of Cu_2O.

Results and discussion

The $Cu_2O(111)$ single crystal sample was grown by using the floating zone method as previously reported.[26,27] The single crystal was oriented with Laue diffraction, cut, and mechanically polished. In order to acquire an atomically flat sample surface for STM measurements, further surface preparation has to be performed under UHV conditions (base pressure: $\sim 1 \times 10^{-11}$ mbar), including argon ion sputtering and 860 K annealing in a low pressure oxygen environment ($\sim 2 \times 10^{-6}$ mbar).[22,28] Compared to the atmospheric conditions used for oxidation,[26,27] this oxygen pressure is very low. Copper vacancies have been predicted as the most energetically favored defects in Cu_2O.[14,26,29] Oxygen vacancies,

though exhibiting poor thermodynamic stability as discussed in the following sections, could form due to the ion sputtering and annealing processes, which are commonly adopted surface treatment techniques to create O vacancies on oxide surfaces.[30,31] After the surface preparation, this sample was transferred into an analysis chamber to perform the LEED and STM characterization under the UHV conditions. Tungsten tips were used for the STM measurements, which were prepared by first electrochemically etching and then degassing in UHV at ~600 K for 3 hours. Bias voltages were applied to the sample. All measurements were performed at room temperature (RT) due to the very low electrical conductivity of the sample at low temperature.

Fig. 1a shows both side and top views of the unrelaxed structural model of the unreconstructed oxygen-terminated $Cu_2O(111)$ surface, in which the Cu_U and O_U ions in the surface layer are indicated in blue and purple in order to differentiate them from the Cu_S and O_S ions in the surface and interior layers. We believe that this stoichiometric surface is the primary (111) surface that we observe after processing; however, as we discuss below, we will also consider the surface with the Cu ions removed. The interatomic spacing of the surface Cu_U ions (and the surface-terminating O_U ions) is 6.1 Å, as shown in the red rhombus in the top view model in Fig. 1a. Fig. 1b shows a LEED pattern acquired from the as-prepared $Cu_2O(111)$ surface. The LEED shows a sharp hexagonal pattern, indicating a large-scale atomically flat surface morphology with a (1×1) periodic atomic construction, consistent with previous results for the surface prepared with the same procedures.[21] Fig. 1c shows a representative large-scale STM topography of the sample surface presenting atomic terraces. The minimum terrace height measured in the STM image is ~2.49 Å, which is consistent with a layer spacing of 2.46 Å from the theoretical model of the (111) surface, as depicted in Fig. 1a.

More features of this surface can be seen when we focus on the terraces. Fig. 1d shows a high-resolution STM image of the atomically flat $Cu_2O(111)$ surface. Three representative surface structures are seen: the pristine (defect-free) surface region (dashed square), triangular dark depressions (dashed triangle) and triangular bright protrusions (solid triangle). Interestingly, all bright defects are found to have the same appearance with a uniform atomic scale size, whereas some dark defects appear as atomic scale defects and some agglomerate into a large dark depression (the larger dashed triangle in Fig. 1d). Moreover, the bright triangular defects are rotated by 180° with respect to the dark triangular defects. These findings suggest that these features are likely to be native structural defects of this (111) surface. We may further exclude unexpected molecular adsorption and surface contamination from the UHV chamber because these dark and bright triangular surface structures remain stable at RT and are not observed to increase or decrease over time in UHV after surface preparation.

Fig. 2a shows an atomically resolved STM image of the pristine surface region, which presents an fcc (111)-like lattice structure, as indicated by the white rhombus with an average side length of ~6.4 Å (averaged from the three directions indicated in Fig. 2b). This spacing rules out the notion that

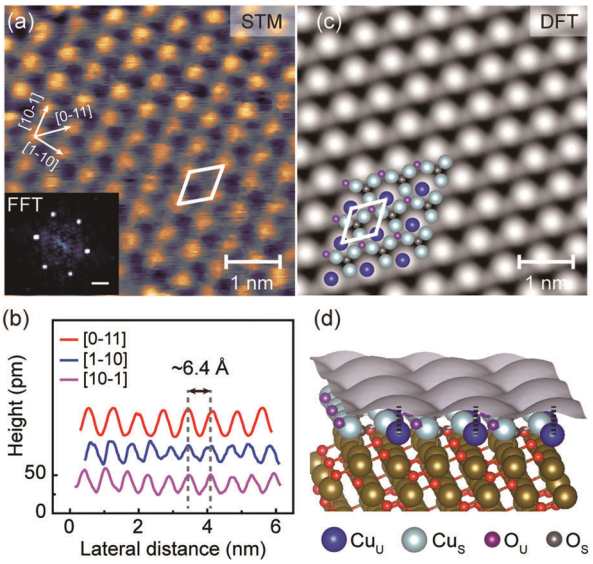

Fig. 2 Atomic structure of the pristine $Cu_2O(111)$-(1×1) surface. (a) High-resolution STM image (+1.5 V, 20 pA, z range: 6.1 Å) of the pristine surface region. Inset: FFT pattern for the STM image. Scale bar: 1 nm^{-1}. (b) Height profiles taken from (a) along three different directions showing an average peak-to-peak separation of ~6.4 Å. (c) DFT-simulated STM image (+1.5 V) of the pristine $Cu_2O(111)$-(1×1) surface, after relaxation. (d) Atomic model of the pristine $Cu_2O(111)$-(1×1) surface overlaid with the DFT-simulated STM image. Black dashed lines show the correspondence of Cu_U ions.

this periodicity corresponds to every Cu atom because the nearest neighboring Cu atoms are spaced by ~3.0 Å in the structural model, as seen in Fig. 2c. Instead, based on the model structures, four scenarios for the origin of these periodic bright protrusions characterized by a rhombic unit with a side length of 6.1 Å appear to be possible. For the stoichiometric (111) surface (Fig. 1a), the protrusions could be due to (1) the outmost O_U ions or (2) the Cu_U ions; for the (111) surface after removing the Cu_U ions, the protrusions could be due to (3) the outmost O_U ions or (4) the triplets of Cu_S ions surrounding the O_S atoms. To explain their observations, Önsten *et al.*[22] suggested that they were observing Cu ions, but were unable to determine which surface they were observing (scenarios (2) and (4)). As we will see below, based on STM measurements combined with DFT-based STM simulations, we believe scenario (2) explains the images, where these protrusions correspond to the Cu_U ions on the stoichiometric (111) surface, as indicated by the model in Fig. 2c. This identification is in agreement with previous findings on few-atomic layer (2–3) thick Cu_2O films on Au.[24]

In order to make this assignment, we simulate the STM images (see Methods for details) for the relaxed DFT structure for both the stoichiometric (111) surface (Fig. 2c) and the (111) surface after removing the Cu_U ions (Fig. S1a, ESI†); these simulations critically consider both the morphology of the surface and the DOS available inside the experimental bias window (V = +1.5 V). While both surfaces reveal periodic protrusions with the expected unit cell, when matched to the underlying model, it is clear that the simulations suggest that the protrusions have different origins for the two surfaces. For

the stoichiometric (111) surface (Fig. 2c), the protrusions are due to the Cu_U ions (scenario (2)); for the (111) surface without Cu_U ions (Fig. S1a, ESI†), however, the protrusions are due to the outmost O_U ions (scenario (3)). This second result bucks the conventional wisdom employed by Önsten *et al.*,[22] which states that the topographic features observed in the STM images will be primarily attributed to the variation of local DOS of surface Cu ions, rather than the outmost O ions on the surface. Previous calculations have shown that the electronic states from O atoms lie far away from the conduction and valence band edges, and the electronic DOS around the Fermi energy (E_F) is primarily dominated by contributions from the 3d electrons of surface Cu atoms.[13,32] While these Cu_S ions are evident in the simulation in Fig. S1a (ESI†), the superior height of the O_U atoms (Fig. 1a) combined with the available DOS due to their empty valence shell allows these ions to dominate the simulated STM image.

We note that after DFT relaxation, the simulated surface Cu_U atoms move slightly downward and transversely, and are no longer at the center of the hexagons formed by Cu_S atoms (Fig. 2c), consistent with previous theoretical studies.[33,34] A detailed comparison between the unrelaxed and relaxed surface structures is presented in Fig. S2 (ESI†). STM image simulation shows that the Cu_U atoms give a bright round contrast pattern with a periodicity of 6.1 Å, in reasonable agreement with the experimental result of ~6.4 Å (the difference may arise from thermal drift, as well as error in the calculated Cu_2O lattice parameters). The correspondence between the positions of high topographic contrast and unsaturated copper ions on the surface is also shown in Fig. 2d.

We now turn to discuss the dark and bright defect features observed on the surface, both to determine their origin and confirm the dominant surface structure. In scenario (2), we identify the bright round protrusions as Cu_U ions; in this case, we can clearly identify the dark triangular defects (Fig. 1d) as missing Cu_U atoms, *i.e.*, Cu_U vacancies, as shown in detail in Fig. 3a (dashed triangles). We performed a DFT relaxation calculation for a model of this Cu_U vacancy (Fig. 3b) and simulated the STM image (Fig. 3c); this prediction agrees well with the experimental STM image. In contrast, if we consider scenario (3), these defects would appear to correspond to O_U vacancies; modelling this structure, performing the DFT calculation and plotting the simulated-STM image reveals features that are completely at odds with observations (Fig. S1b, ESI†). Instead of revealing depressions at the vacancy sites, the uncovered Cu ions and their available DOS close to the Fermi level produce new protrusions that dominate the simulated topography. This result is exactly opposite to the observations and rules out scenario (3), leaving us with scenario (2) as the only reasonable explanation for our observations.

In light of this assignment, we examine the bright triangular defects in Fig. 3a (solid triangles). In contrast to the Cu_U vacancies, these defects show completely different atomic-scale features consisting of three smaller bright Cu_U ions that appear to be drawn closer together, forming dark depressions around them. As shown in Fig. 3d, between the three nearest Cu_U atoms (black triangle), there should exist an O_U ion (purple) bonded with other three neighboring Cu_S ions. We built an atomic model by removing every third O_U ion along each direction of O rows on the surface, indicated by the purple arrow, and optimized the resulting structure using DFT; this O_U ion vacancy was proposed to be a possible defect structure which produced the (111) $(\sqrt{3} \times \sqrt{3})R30^\circ$ reconstructed surface.[22] As shown in Fig. 3e, the optimized atomic structure after the removal of one-third of the surface O_U ions shows that the three nearest Cu_U ions are pulled together, significantly reducing the interatomic-distance from 6.1 Å to 5.0 Å; this is consistent with the experimental observation of 4.7 Å. These simulated features (V = +1.5 V) are also rotated by 180° with respect to the Cu_U vacancies in accordance with the observations. Simulations for

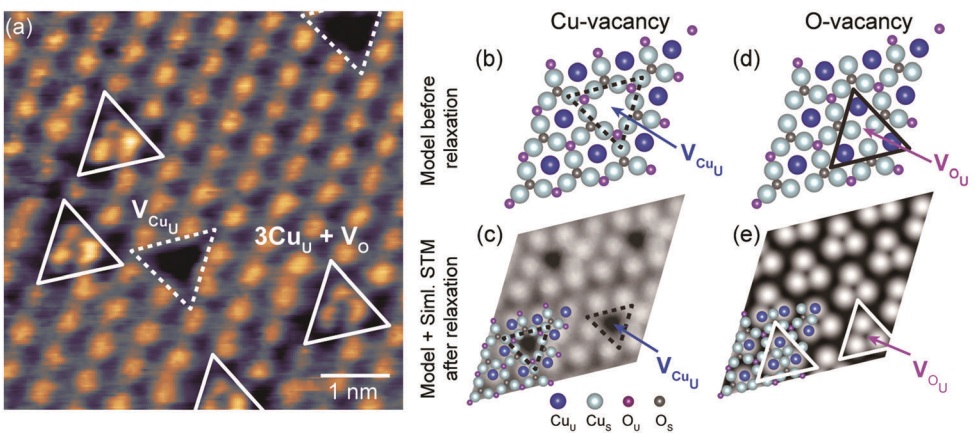

Fig. 3 Atomic structure of native defects of the $Cu_2O(111)$ surface. (a) High-resolution STM image (+1.5 V, 20 pA, z range: 11 Å) of a representative defective surface region, containing the dark and bright triangular defects. (b) Structural model of a surface Cu_U vacancy (V_{Cu_U}, dashed triangles) without any structural relaxation. Only surface layer atoms are shown and denoted. (c) DFT-simulated STM image (+1.5 V) of the surface model shown in (b) after structural relaxation. (d) and (e) Same as (b) and (c) but for the surface V_O vacancy (V_{O_U}). The relaxed atomic structure is also overlaid on the simulated image. After relaxation, the three nearest neighboring Cu_U have moved towards the center of the oxygen vacancy, forming a shrunken triangular pattern shown as a white solid triangle.

an isolated O_U vacancy, both at the positive (V = +1.5 V, Fig. S3a, ESI†) and the negative (V = −1.5 V and Fig. S3b, ESI†) bias, are also consistent with the observed structures in Fig. 3a and 1d, respectively. Therefore, the atomic-scale imaging and DFT calculations argue that each bright triangular defect contains an O_U vacancy in the center (and further support the assignment of scenario (2)).

Based on our identification, it appears that 'isolated' Cu_U and O_U vacancies coexist on the same surface, in some cases separated by only ∼2 nm (Fig. 3a). While Cu vacancies are well-known to form in bulk[20,26] and lead to the p-type behavior of Cu_2O crystals, O vacancies are not as frequently reported.[35] We calculated the formation energies of isolated and paired surface defects under oxygen-poor conditions (details in the ESI,† Fig. S4). We find that surface Cu vacancies are spontaneous (with a formation energy of −0.6 eV), but surface O vacancies have a high formation energy of +1.4 eV, making their formation thermodynamically rare. Oxygen vacancies are likely generated through the sputtering process and persist because they have no path to resolution in the UHV environment.[22] It is worth noting that the negative formation energy of Cu vacancies indicates that the Cu_U vacant surface is thermodynamically favorable, but previous DFT calculations have also shown that the stoichiometric Cu-terminated surface only has marginally higher surface energy than the Cu_U vacant surface under high vacuum conditions.[14,20] Moreover, the formation of a large-scale Cu_U vacant surface may be hindered by kinetic factors in spite of its thermodynamic favorability. It was concluded through the comparison between experimental and simulated STM images that the Cu-terminated surface is what we have observed experimentally.

We were also interested in the energetic stability of pairs or assemblies of defects. Clearly, Cu_U vacancies (possibly combined with O_U vacancies) appear to congregate into the larger vacancy islands shown in Fig. 1d. Conversely, the bright protrusions identified as associated with O vacancies do not appear to congregate – in fact, they may even 'repel' one another. We tested this hypothesis by creating a binary image by thresholding the data by height in Fig. 1d and performing a 2D auto-correlation function (details in Section S5 of the ESI†). Indeed, the auto-correlation function (shown in Fig. 1e) shows a significant dip at nearest neighbor sites and next nearest neighbor sites along the primary axes, indicating that these bright protrusions – identified as the O_U vacancies – are unlikely to be found close to one another. This relative repulsion may be explained by the charge on these defects; previous DFT calculations[36] showed that in the bulk, Cu vacancies are likely neutral while O vacancies are positively charged.

Having determined the atomic structures of pristine and defective surfaces, we turn to examine the electronic properties of these surfaces in order to gain insight into the electronic states that determine the experimental observations. We characterized

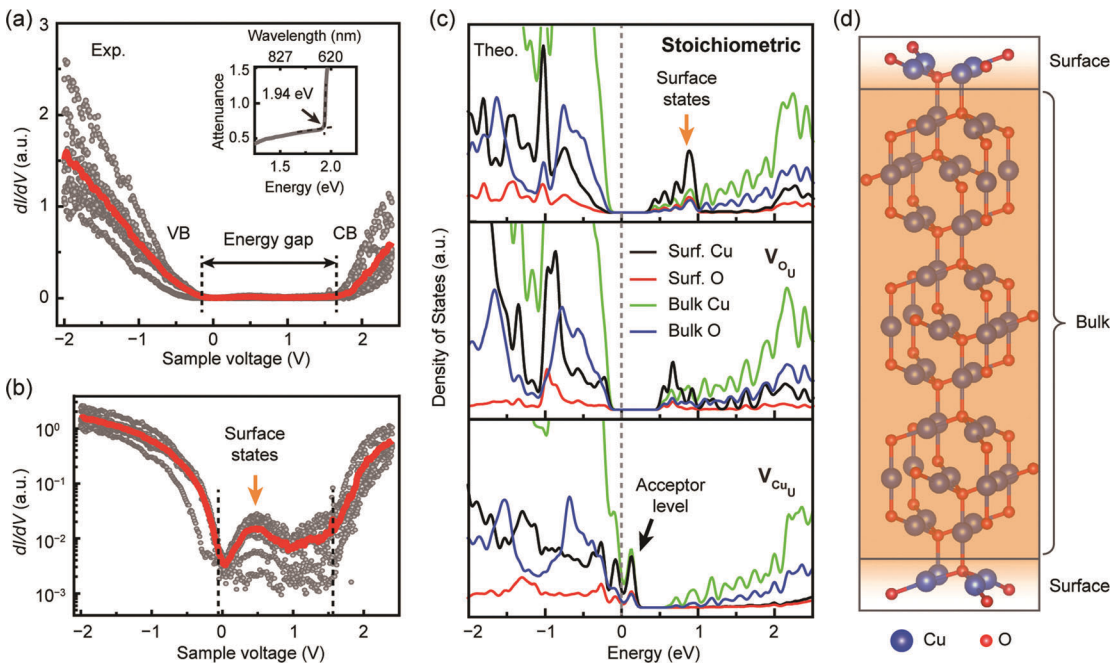

Fig. 4 Electronic structure of the $Cu_2O(111)$ surface. (a) Averaged experimental dI/dV curve (red) measured at the different sites (gray) on the $Cu_2O(111)$ surface. The inset shows an optical attenuance spectrum of the Cu_2O single crystal. (b) Detailed plot of (a) on a logarithmic scale. (c) DFT-calculated density of states (DOS) of the surface and bulk of the $Cu_2O(111)$ system shown in (d) with the surface termination of the stoichiometric (1 × 1) structure (top panel), the (1 × 1) surface without O_U ions (middle), and the (1 × 1) surface without Cu_U ions (bottom). The energy is reported to be relative to the valence band maximum, which is close to the Fermi energy (E_F) in Cu_2O. The black, red, green, and blue curves in each panel represent the DOS dispersion of surface Cu, surface O, bulk Cu, and bulk O species with energy, respectively. The orange and black arrows indicate the positions of the surface states related to the surface Cu_U ions, and the acceptor level associated with the Cu_U-vacancies on the surface, respectively. (d) The Cu_2O structure for the DOS calculation. Both top and bottom layers of Cu_2O are considered the surfaces, and the nine middle layers are considered the bulk.

the electronic structure of this crystalline surface by STS (Fig. 4a). It was challenging to precisely acquire isolated dI/dV spectra for all these featured surface structures, *e.g.* the vacancies of Cu_U and O_U ions, due to the poor electrical conductivity and stability of the surface structures (and the requirement of working at room temperature). The dI/dV spectra measured at various sites on the surface (which may include the Cu_U and O_U vacancies) are generally characterized by global features including the wide energy band gap. The band gap evaluated from the averaged dI/dV spectrum (the red curve in Fig. 4a) at RT is $\sim$1.6–2.1 eV, which is consistent with the onset of optical absorption at 1.94 eV observed in the attenuance spectrum (inset, Fig. 4a) taken on the same sample.

Additionally, at certain points on the surface, a weak and broad dI/dV peak is seen at $\sim$0.5 eV above E_F in the band gap (Fig. 4b). Previous STS measurements on few-atomic-layer Cu_2O on Au have also revealed a peak in the band gap, which the authors attributed to mixed Cu_U and O_U character.[24] However, it is not clear whether the peak we observed (Fig. 4b) has the same origin; the peak from the few-atomic-layer sample was observed at the conduction band edge and dominated the spectrum,[24] while for our single-crystalline sample, the peak resides in the middle of the band gap and can only be resolved on a log scale. In order to explain our observation, we performed DFT calculations (Fig. 4c) for a symmetrical Cu_2O slab consisting of eleven stoichiometric Cu_2O atomic layers along the surface normal direction (Fig. 4d) in order to analyze the dependency of the DOS with ion species and the tendency of the DOS change with the surface defects. The top and bottom layers are considered as the surfaces, and the interior is considered as the bulk region. Three surface structures, *i.e.* the stoichiometric (1×1) surface, the (1×1) surface without O_U ions (V_{O_U} surface) and the (1×1) surface without Cu_U ions (V_{Cu_U} surface), were evaluated. These calculations are able to provide a qualitative description of the energy states in the gap, although the magnitude of the Cu_2O band gap is significantly underestimated by DFT using GGA functionals.[19,37,38] As shown in Fig. 4c, the stoichiometric surface (top panel) and the surface without O_U ions (middle panel) show very a similar electronic structure in which they present a wide gap feature and the in-gap states (orange arrow) at $\sim$0.8 eV above E_F. The in-gap peak is shifted to lower energy for the O_U vacant surface as compared to the stoichiometric surface. However, these in-gap features disappear for the surface without Cu_U ions (bottom panel), indicating that these states largely stem from the Cu_U ions on the surface, consistent with the results reported previously.[24,32] Moreover, the calculation also shows that the surface without Cu_U ions presents extra electronic states around E_F (black arrow), qualitatively consistent with the acceptor level associated with Cu vacancies in Cu_2O crystals examined by either optical spectroscopy or theoretical calculations, which is usually slightly ($\sim$0.4 eV) higher than the valence band maximum.[20,39] However, we did not see such distinct acceptor energy levels on the experimental dI/dV curves, likely because they are affected by thermal broadening at RT and/or tip effects, overlaid with the valence band, or simply undersampled in the measurements.

Conclusions

In summary, we studied the atomic structure of the $Cu_2O(111)$ surface by STM imaging combined with DFT calculations and simulations. We determined that the Cu_U ions on the surface are observable as bright protrusions under STM. Two types of surface defects, vacancies of Cu and O ions, were also identified. The Cu vacancies appear as depressions under STM while the O vacancies attract three neighboring Cu_U ions together, forming a brighter triangular defect structure oriented in the opposite direction. The electronic band gap of a single crystalline surface revealed by dI/dV spectroscopy was estimated to be within the range of $\sim$1.6–2.1 eV. Moreover, extra in-gap electronic states were also observed to form near the E_F in both dI/dV spectroscopy and DFT calculations, which were assigned to the surface states stemming from the unsaturated surface Cu ions. The surface defect structures (O_U and Cu_U vacancies) were further predicted to shift the energy level of these in-gap states or introduce more acceptor levels, which could provide more actively binding sites for gas molecules to react on the surface.

Methods

The Cu_2O crystal was grown by oxidizing high-purity copper rods and crystallizing it with the floating zone method.[26] The (111) crystalline orientation was determined with Laue diffraction and then prepared by mechanical cutting and polishing. This surface was further processed under UHV conditions with Ar^+ ion sputtering (1.0 kV) and high-temperature annealing (860 K) in oxygen (oxygen pressure: $\sim 2 \times 10^{-6}$ mbar) for 30 minutes. LEED and STM experiments were performed under UHV conditions (base pressure: 1×10^{-11} mbar) in a commercial UHV chamber (Omicron) with a home-built STM microscope. Electrochemically etched tungsten tips were used for the STM imaging and tunnelling spectroscopy measurements. We further degassed the tip at 600 K for 3 hours, and cleaned and inspected it on a clean Cu metal surface by imaging and dI/dV spectroscopy. Lock-in detection was used to extract the effect of a 30 mV amplitude 20 kHz voltage modulation that was added to the DC sample voltage for dI/dV measurements.

The Vienna Ab initio Simulation Package (VASP)[40,41] was used to perform DFT calculations to simulate the surface geometries and STM images of various $Cu_2O(111)$ surface types. Projector-augmented wave (PAW)[42] atomic potentials were used in conjunction with a cutoff energy of 400 eV for the plane-wave basis set. The generalized-gradient approximation (GGA) with the parametrization of Perdew–Burke–Ernzerhof (PBE) was used for the exchange–correlation functional.[43] On-site Coulomb interaction between the localized 3d electrons was accounted for using the DFT+U approach proposed by Dudarev,[44] with a U–J value of 4 eV applied on Cu, as calibrated by Wang *et al.*[45] The calculated Cu_2O lattice parameter was 4.30 Å, in close agreement with the experimental value of 4.27 Å.[46] The Kohn–Sham gap of bulk Cu_2O was found to be 0.64 eV, in comparison with the experimental value of 2.17 eV.[47,48]

STM images were obtained within the Tersoff–-Hamann approximation,[49] in which the constant current STM image is modeled as a surface of constant charge density from Kohn–Sham eigenstates corresponding to eigenenergies within a certain range. Asymmetric $Cu_2O(111)$ surface slabs were used for STM simulation, which consisted of five O–Cu–O trilayers. A trilayer is defined as one layer of Cu atoms between two O layers.[50] A vacuum spacing of approximately 15 Å separates each slab from its periodic images to prevent unphysical coupling. The positions of all atoms, except the bottom trilayer, were allowed to relax in all three directions until the force components acting on each atom were less than 0.01 eV $Å^{-1}$. All calculations were spin polarized. The Brillouin zone was sampled using a $6 \times 6 \times 1$ Monkhorst–Pack[51] grid for the vacancy-free 1×1 surfaces. Surfaces containing Cu or O vacancies were modeled using 3×3 surfaces with a $2 \times 2 \times 1$ Monkhorst–Pack grid. Density of states (DOS) calculations used symmetric surface slabs consisting of 11 trilayers with all atoms being allowed to relax. Electron smearing was carried out using Gaussian smearing with a width of 0.05 eV. Convergence tests were performed by varying the computational parameters such as the slab thickness, planewave cutoff energy, Brillouin zone sampling grid and vacuum size.

Conflicts of interest

The authors declare no conflict of interest.

Acknowledgements

Use of the Center for Nanoscale Materials, an Office of Science user facility, was supported by the U.S. Department of Energy, Office of Science, Office of Basic Energy Sciences, under Contract No. DE-AC02-06CH11357. This material is based on work supported by Laboratory Directed Research and Development (LDRD) funding from Argonne National Laboratory, provided by the Director, Office of Science, of the U.S. Department of Energy under Contract No. DE-AC02-06CH11357. Support for this work was also provided by the Department of Energy Office of Basic Energy Sciences (SISGR Grant DE-FG02-09ER16109). Crystal growth was supported by funding from the National Science Foundation (DMR-1608218). The computing resources provided on Bebop, a high-performance computing cluster operated by the Laboratory Computing Resource Center at Argonne National Laboratory are gratefully acknowledged, as is the National Energy Research Scientific Computing Center (NERSC), a DOE Office of Science User Facility supported by the Office of Science of the U.S. Department of Energy under Contract No. DE AC02-05CH11231. L. F. acknowledges NSF IGERT DGE-0801685, the J. B. Cohen X-Ray Diffraction Facility and Optical Microscopy and Metallography Facility supported by the MRSEC program of the National Science Foundation (DMR-1121262) at the Materials Research Center of Northwestern University, and the Australian Research Council Centre of Excellence in Exciton Science (CE170100026).

Notes and references

1 I. Sullivan, B. Zoellner and P. A. Maggard, *Chem. Mater.*, 2016, **28**, 5999–6016.
2 R. Wick and S. D. Tilley, *J. Phys. Chem. C*, 2015, **119**, 26243–26257.
3 J. Kaur, O. Bethge, R. A. Wibowo, N. Bansal, M. Bauch, R. Hamid, E. Bertagnolli and T. Dimopoulos, *Sol. Energy Mater. Sol. Cells*, 2017, **161**, 449–459.
4 J. Luo, L. Steier, M. K. Son, M. Schreier, M. T. Mayer and M. Grätzel, *Nano Lett.*, 2016, **16**, 1848–1857.
5 Q. Zhai, S. Xie, W. Fan, Q. Zhang, Y. Wang, W. Deng and Y. Wang, *Angew. Chem., Int. Ed.*, 2013, **52**, 5776–5779.
6 X. Chang, T. Wang, P. Zhang, Y. Wei, J. Zhao and J. Gong, *Angew. Chem., Int. Ed.*, 2016, **55**, 8840–8845.
7 E. L. Uzunova, N. Seriani and H. Mikosch, *Phys. Chem. Chem. Phys.*, 2015, **17**, 11088–11094.
8 Z. Besharat, J. Halldin Stenlid, M. Soldemo, K. Marks, A. Önsten, M. Johnson, H. Öström, J. Weissenrieder, T. Brinck and M. Göthelid, *J. Chem. Phys.*, 2017, **146**, 244702.
9 M. Soldemo, J. H. Stenlid, Z. Besharat, N. Johansson, A. Önsten, J. Knudsen, J. Schnadt, M. Göthelid, T. Brinck and J. Weissenrieder, *J. Phys. Chem. C*, 2017, **121**, 24011–24024.
10 A. Soon, M. Todorova, B. Delley and C. Stampfl, *Surf. Sci.*, 2007, **601**, 5809–5813.
11 E. I. Solomon, P. M. Jones and J. A. May, *Chem. Rev.*, 1993, **93**, 2623–2644.
12 G. P. Vissokov, *Catal. Today*, 2004, **89**, 223–231.
13 B.-Z. Sun, W.-K. Chen and Y.-J. Xu, *J. Chem. Phys.*, 2010, **133**, 154502.
14 L. I. Bendavid and E. A. Carter, *J. Phys. Chem. B*, 2013, **117**, 15750–15760.
15 R. Zhang, H. Liu, H. Zheng, L. Ling, Z. Li and B. Wang, *Appl. Surf. Sci.*, 2011, **257**, 4787–4794.
16 A. Soon, M. Todorova, B. Delley and C. Stampfl, *Phys. Rev. B: Condens. Matter Mater. Phys.*, 2007, **75**, 125420.
17 A. Soon, X. Y. Cui, B. Delley, S. H. Wei and C. Stampfl, *Phys. Rev. B: Condens. Matter Mater. Phys.*, 2009, **79**, 035205.
18 M. M. Islam, B. Diawara, V. Maurice and P. Marcus, *THEOCHEM*, 2009, **903**, 41–48.
19 L. Y. Isseroff and E. A. Carter, *Phys. Rev. B: Condens. Matter Mater. Phys.*, 2012, **85**, 235142.
20 D. O. Scanlon, B. J. Morgan, G. W. Watson and A. Walsh, *Phys. Rev. Lett.*, 2009, **103**, 096405.
21 K. H. Schulz and D. F. Cox, *Phys. Rev. B: Condens. Matter Mater. Phys.*, 1991, **43**, 1610.
22 A. Önsten, M. Göthelid and U. O. Karlsson, *Surf. Sci.*, 2009, **603**, 257–264.
23 H. Sträter, H. Fedderwitz, B. Groß and N. Nilius, *J. Phys. Chem. C*, 2015, **119**, 5975–5981.
24 N. Nilius, H. Fedderwitz, B. Groß, C. Noguera and J. Goniakowski, *Phys. Chem. Chem. Phys.*, 2016, **18**, 6729–6733.
25 C. Möller, H. Fedderwitz, C. Noguera, J. Goniakowski and N. Nilius, *Phys. Chem. Chem. Phys.*, 2018, **20**, 5636–5643.
26 K. B. Chang, L. Frazer, J. J. Schwartz, J. B. Ketterson and K. R. Poeppelmeier, *Cryst. Growth Des.*, 2013, **13**, 4914–4922.

27 L. Frazer, K. B. Chang, K. R. Poeppelmeier and J. B. Ketterson, *Sci. Technol. Adv. Mater.*, 2015, **16**, 034901.
28 A. Önsten, J. Weissenrieder, D. Stoltz, S. Yu, M. Göthelid and U. O. Karlsson, *J. Phys. Chem. C*, 2013, **117**, 19357–19364.
29 L. Frazer, E. J. Lenferink, K. B. Chang, K. R. Poeppelmeier, N. P. Stern and J. B. Ketterson, *J. Lumin.*, 2015, **159**, 294–302.
30 S. Tan, Y. Zhao, J. Zhao, Z. Wang, C. Ma, A. Zhao, B. Wang, Y. Luo, J. Yang and J. Hou, *Phys. Rev. B: Condens. Matter Mater. Phys.*, 2011, **84**, 6–10.
31 T. L. Thompson and J. T. Yates, *Top. Catal.*, 2005, **35**, 197–210.
32 A. Soon, T. Söhnel and H. Idriss, *Surf. Sci.*, 2005, **579**, 131–140.
33 Y. Shen, F. H. Tian, S. Chen, Z. Ma, L. Zhao and X. Jia, *Appl. Surf. Sci.*, 2014, **288**, 452–457.
34 H. Xu, B. Miao, M. Zhang, Y. Chen and L. Wang, *Phys. Chem. Chem. Phys.*, 2017, **19**, 26210–26220.
35 D. O. Scanlon and G. W. Watson, *J. Phys. Chem. Lett.*, 2010, **1**, 2582–2585.
36 M. Nolan, *Thin Solid Films*, 2008, **516**, 8130–8135.
37 S. Lany, *Phys. Rev. B: Condens. Matter Mater. Phys.*, 2013, **87**, 085112.
38 L. Li, R. Zhang, J. Vinson, E. L. Shirley, J. P. Greeley, J. R. Guest and M. K. Y. Chan, *Chem. Mater.*, 2018, **30**, 1912–1923.
39 N. Harukawa, S. Murakami, S. Tamon, S. Ijuin, A. Ohmori, K. Abe and T. Shigenari, *J. Lumin.*, 2000, **87**, 1231–1233.
40 G. Kresse and J. Furthmüller, *Comput. Mater. Sci.*, 1996, **6**, 15–50.
41 G. Kresse and J. Furthmüller, *Phys. Rev. B: Condens. Matter Mater. Phys.*, 1996, **54**, 11169–11186.
42 G. Kresse and D. Joubert, *Phys. Rev. B: Condens. Matter Mater. Phys.*, 1999, **59**, 1758–1775.
43 J. P. Perdew, K. Burke and M. Ernzerhof, *Phys. Rev. Lett.*, 1996, **77**, 3865–3868.
44 S. Dudarev and G. Botton, *Phys. Rev. B: Condens. Matter Mater. Phys.*, 1998, **57**, 1505–1509.
45 L. Wang, T. Maxisch and G. Ceder, *Phys. Rev. B: Condens. Matter Mater. Phys.*, 2006, **73**, 195107.
46 A. Werner and H. D. Hochheimer, *Phys. Rev. B: Condens. Matter Mater. Phys.*, 1982, **25**, 5929–5934.
47 B. K. Meyer, A. Polity, D. Reppin, M. Becker, P. Hering, P. J. Klar, T. Sander, C. Reindl, J. Benz, M. Eickhoff, C. Heiliger, M. Heinemann, J. Bläsing, A. Krost, S. Shokovets, C. Müller and C. Ronning, *Phys. Status Solidi B*, 2012, **249**, 1487–1509.
48 T. Kazimierczuk, D. Fröhlich, S. Scheel, H. Stolz and M. Bayer, *Nature*, 2014, **514**, 343–347.
49 J. Tersoff and D. Hamann, *Phys. Rev. Lett.*, 1983, **50**, 1998.
50 L. I. Bendavid and E. A. Carter, *J. Phys. Chem. C*, 2013, **117**, 26048–26059.
51 H. J. Monkhorst and J. D. Pack, *Phys. Rev. B: Solid State*, 1976, **13**, 5188–5192.